Title

Turbulent Kinetic Energy Budgets over Gentle Topography Covered by Forests

Journal

Journal of the Atmospheric Sciences, 80(1)

ISSN

0022-4928

Authors

Chen, Bicheng
Chamecki, Marcelo

Publication Date

2023

DOI

10.1175/jas-d-22-0027.1

Turbulent kinetic energy budgets over gentle topography covered by forests

Bicheng Chen[a] and Marcelo Chamecki[b]

[a] *Department of Physical Oceanography, College of Ocean and Earth Sciences, Xiamen University, China*

[b] *Department of Atmospheric and Oceanic Sciences, University of California Los Angeles, Los Angeles, California, USA*

Corresponding author: Marcelo Chamecki, chamecki@ucla.edu

ABSTRACT: Large eddy simulations of flow over a “horizontally” uniform model forest are used to investigate the effects of gentle topography on the turbulent kinetic energy (TKE) budget within the canopy roughness sublayer. Despite significant differences between simulations using idealized sinusoidal topography and real topography of the Amazon forest, results indicate that the effects of topography are located predominantly in the upper canopy and above, and are mostly caused by mean advection of TKE. The “horizontally” averaged TKE budget from idealized and real gentle topographies are almost identical to that for flat terrain, including a clear inertial layer above the roughness sublayer in which shear production is balanced by local dissipation. At topography crests, where observational towers are usually located, mean vertical advection of TKE can be as important as horizontal advection. We propose the use on an approximate TKE balance equation to estimate mean advection from single tower measurements, and introduce a new advection index that can be used as a proxy to quantify the importance of the topography on the TKE budget.

1. Introduction

Turbulence and flux measurements over forests in complex terrain are of great importance in our understanding of surface-atmosphere interactions. These measurements are often interpreted in the framework developed for flat terrain. This is particularly true when the topography is gentle. However, it has long been known that dense canopies such as forests enhance the effects of topography on the flow (Ruck and Adams 1991; Finnigan and Belcher 2004; Ross and Vosper 2005), and even when forests sit on gentle topography the flow is often characterized by recirculation zones "hidden" inside the forest. The flow modifications induced by topography have a large impact on the spatial redistribution of gases and on the interpretation of eddy covariance measurements (Katul et al. 2006; Poggi and Katul 2007; Ross 2011; Ross and Harman 2015; Chen et al. 2019, 2020). The lack of a better framework to interpret these measurements stems, in part, from the difficulty in making spatial observations needed to study non-homogeneous flows over complex terrain. Large eddy simulation (LES) has expanded significantly our ability to study these flows (e.g. Brown et al. 2001; Tamura et al. 2007; Ross 2008; Dupont et al. 2008; Patton and Katul 2009; Ross 2011; Chen et al. 2019, 2020).

One difficulty in most observational studies in gentle terrain is that it is hard to assess the importance of the effects of topography on the flow. In neutral flow over rough topography, any deviation from the log-law in the observed mean velocity profile can be attributed to the effects of topography (e.g., the speed-up maximum that is present above the crest). However, for observational data collected over forested topography, canopy drag and atmospheric stability also impact the shape of the mean velocity profile, and the effect of gentle topography may not be strong enough to be unambiguously identified. In addition, in many cases, measurements are not made far enough above the canopy for the effects of the topography to be discernible. As an example, observations of vertical profiles of mean velocity from the Amazon forest over gentle topography do not show the usual speed-up maxima that would clearly indicate effects of the topography on the flow (e.g., see profiles in Kruijt et al. 2000; Gerken et al. 2017; Santana et al. 2018) and it is hard to assess deviations from the flat terrain profile without having an upwind profile for reference (and using a locally determined friction velocity). As an example, Gerken et al. (2017) found good agreement between observed mean velocity profiles in the Amazon and LES results for a model forest over flat terrain.

In a recent study, Chamecki et al. (2020) showed that the turbulent kinetic energy (TKE) budget estimated from single tower observations may contain enough information to identify (and possibly quantify) the effects of topography on the flow. Using tower data from two sites in the Amazon forest they identified a region above the canopy in which TKE production is smaller than dissipation. This pattern is inconsistent with our current understanding of the TKE budget over flat topography, as production is expected to be larger than dissipation in the roughness sublayer above the canopy (Brunet et al. 1994; Pan and Chamecki 2016) and in the lower portion of the mixed layer (Lenschow et al. 1980). Chamecki et al. (2020) concluded that the observed pattern of production being smaller than dissipation could only be explained by deviations from horizontal homogeneity, which in the case of the two Amazon forest sites was likely caused by the topography. They also showed that this feature was in agreement with LES of forests over sinusoidal topography.

Results from Chamecki et al. (2020) suggest that it may be possible to use the TKE budget to characterize effects of topography using single tower measurements. However, a better understanding of the TKE budget in the roughness sublayer over complex terrain is needed to guide the interpretation of field observations. Here we use LES to contrast and interpret TKE budgets over identical "horizontally" uniform model forests sitting on 3 different topographies: flat, idealized sinusoidal ridges, and real topography. We focus the data analysis on two main questions: (1) how does gentle topography alter the TKE budget in the canopy roughness layer? and (2) how do we interpret tower observations usually sited on the crests of the topography? We also discuss some observational issues that must be addressed before this framework can be applied to field data.

2. Methods

a. Specific terminology

It is traditional in ABL studies to distinguish horizontal and vertical directions, given the different scales and processes that characterize these spatial dimensions. In the presence of topography, this distinction becomes less clear because there are several coordinate systems that can be used to describe the flow (e.g., terrain-following or streamline coordinate systems). In the present work, we will use the term "horizontal" (with quotation marks) to refer to terrain-following surfaces (i.e., surfaces parallel to the topography at a constant distance from the ground), so that "horizontal" averaging and "horizontal" homogeneity refer to averaging over and uniformity across terrain-following surfaces. When the analysis is restricted to the crests and troughs of topography where towers are usually sited, the distinction between the different coordinate systems is eliminated, and the terms vertical and horizontal retain their original meaning (no quotation marks are used). In these instances, we will always explicitly refer to troughs and crests for the sake of clairty.

b. Numerical model

We used the LES model described by Chen et al. (2019) to simulate a "horizontally" homogeneous model forest on three distinct topographies. The numerical model combines a pseudo-spectral discretization with full dealiasing using the 3/2 rule in the horizontal directions with a staggered second-order centered finite-difference scheme in the vertical (Albertson and Parlange 1999). The LES combines a distributed drag force modeled by the quadratic drag law to represent the main effects of the canopy on the flow (Shaw and Schumann 1992; Pan et al. 2014) with an immersed boundary method to represent the topography on a cartesian uniform grid (Peskin 1972; Chester et al. 2007). The immersed boundary method uses a signed-distance function to represent the ground surface and a second-order accurate smoothing method (Li et al. 2016) to reduce the Gibbs phenomenon at the fluid-solid interface caused by the horizontal pseudo-spectral discretization (more details of the IBM implementation are presented in Appendix A). A stress-free no-penetration boundary conditions is applied at the top of the domain. The SGS momentum flux is parameterized using the Smagorinsky-Lilly model (Smagorinsky 1963; Lilly 1967), with the Smagorinsky coefficient determined dynamically using the Lagrangian scale-dependent dynamic model (Bou-Zeid et al. 2005). The system is integrated in time using the second-order Adams-Bashforth scheme. The reader is referred to Albertson and Parlange (1999), Bou-Zeid et al. (2005), Pan et al. (2014), Chen et al. (2019), and Appendix A for more details of the code. Our LES model implementation has been extensively validated for a wide range of flow conditions, including comparisons with tower observations for flow within and above plant canopies over flat topography (Pan et al. 2014; Gerken et al. 2017; Lin et al. 2018) and comparisons with high-resolution wall-resolved LES for flow over topography (see appendix in Heisel et al. 2021).

c. Simulation setup

The three main simulations employed here were presented in detail by Chen et al. (2020), and we only give a brief description here. The forest canopy was designed to represent the Amazon forest near the K34 research tower (Tóta et al. 2012; Fuentes et al. 2016), even though the K34 tower location is not included in the domain. The model canopy was assumed to be "horizontally" homogeneous and continuous across the entire domain, with a leaf area density (LAD) profile $a(z)$ based on data from Tóta et al. (2012) reported in Fuentes et al. (2016), and with total leaf area index $LAI = 7\ \mathrm{m}^2/\mathrm{m}^2$. The canopy height was $h_c = 39\,\mathrm{m}$, resulting in an adjustment length $L_c = 1/(C_d\overline{a}) = 13.9$ m, where $\overline{a} = 0.18\ \mathrm{m}^{-1}$ was the average LAD of the canopy and C_d was the drag coefficient assumed constant. The three simulations differ on the topography: simulation "Flat" has no topography and serve as a benchmark for the canonical canopy flow, simulation "Idealized" has a simple topography with sinusoidal ridges, and simulation "Real" uses a small region of the real topography of the Amazon forest (centered at $-2.413°$ S, $-60.504°$ W) and shown in Fig. 1 (this topography was extracted from a large area with reasonably similar topography and, given the periodic boundary conditions implied by the spectral discretization, this simulation is interpreted here as a simulation of a very large area with similar topographic features). The idealized topography case has a ridge height (twice of the amplitude of the cosine function) $H = 50$ m and a ridge half-length (one fourth of the topography wavelength) $L = 250$ m (resulting in an average slope $H/L = 0.2$), which are comparable to the typical topography in the Amazon forest around the K34 tower. For both the idealized and real topographies the forest is considered a deep canopy because $h_c/L_c > 1$ (Finnigan and Belcher 2004; Poggi et al. 2008). For some specific analyses we also include two additional idealized simulations reported by Chen et al. (2019) with the same hill half-length but with half the hill height (simulation "Half" with $H = 25$ m and slope $H/L = 0.1$) and twice the hill height (simulation "Double" with $H = 100$ m and slope $H/L = 0.4$ – note that because of the large slope this case is no longer considered gentle topography). For the idealized topography and the dominant topographic features of the real topography, the flow is in the long-hill regime ($L/L_c \gg 1$) in which the turbulence is approximately in local equilibrium with the local shear (Poggi et al. 2008; Chen et al. 2019). Due the the varying position of the ground surface within the cartesian grid, the vertical position between the grid nodes within the LAD profile vary within the domain. Our approach to represent the canopy on the cartesian grid consisted of obtaining values of LAD by interpolating the LAD profile to the heigh of each node (with respect to the ground surface) and renormalizing the final profile to match the total LAI. This means that if the top of the canopy is below a given node, that node has zero LAD. While this treatment of the canopy could be problematic in some cases (e.g. creating large horizontal gradients in LAD), in our setup the canopy density above $z = 30\,\mathrm{m}$ is very small and the vertical grid resolution is fine enough to resolve the vertical gradients in LAD. All simulations were carried out under neutral stratification and were driven by a constant mean pressure gradient force (per unit mass) equal to 3.11×10^{-4} m/s^2 in the streamwise direction. For the simulation without topography, this forcing resulted in a friction velocity of approximately 0.4 m/s (hereafter we refer to this as the equivalent friction velocity, and use it as a normalization value for all simulations). Simulations were integrated for 5 hours in total with a time step of 0.1 seconds, and data analysis was performed using the last 2 hours. For the "Real" case in which no spatial averaging is possible, simulations were carried our for 8 hours and data analysis used the final 5 hours. Details of the domain size and grid resolution for each simulation are listed in Table 1 and discussed in detail in Appendix B.

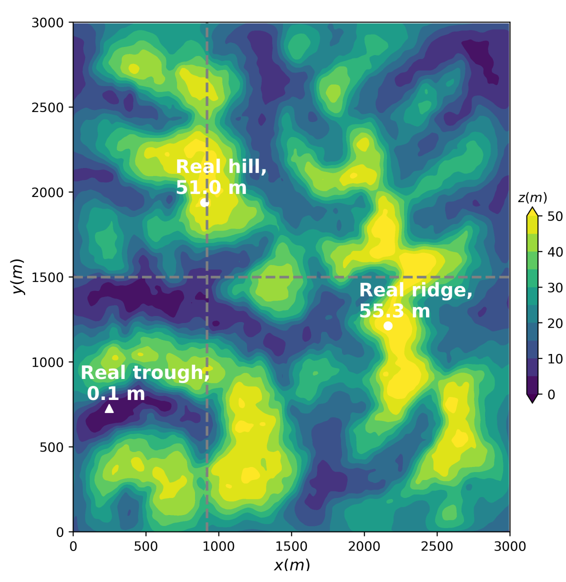

FIG. 1. Topography map of a portion of central Amazonia used for the "Real" simulation. The 3 virtual towers selected for detailed analysis are shown by black circles and the positions of cross sections used in later figures are indicated by dashed lines.

Variables (all in m)	“Flat”	“Idealized”	“Real”
Streamwise domain size	2000	2000	3000
Crosswise domain size	1000	1000	3000
Vertical domain size	515	540	540
Horizontal grid resolution	6.25	6.25	8
Vertical grid resolution	2	2	2
Mean topography height	0	25.00	26.46

TABLE 1. Domain and grid configuration used in numerical simulations.

d. Data analysis

We define the resolved TKE as

$$\overline{e} = \frac{1}{2}\overline{\widetilde{u_i}'\widetilde{u_i}'} \tag{1}$$

where $\widetilde{\mathbf{u}}$ is the resolved portion of the velocity resulting from the implicit filtering operation in the numerical model, which is further decomposed into ensemble average and fluctuations as $\widetilde{\mathbf{u}} = \overline{\widetilde{\mathbf{u}}} + \widetilde{\mathbf{u}}'$. The analysis presented here is based on the budget of resolved TKE which is given by (Dwyer et al. 1997; Yue et al. 2008)

$$\begin{aligned} \frac{\partial \overline{e}}{\partial t} = & \underbrace{-\frac{\partial \overline{\widetilde{u}}_j\,\overline{e}}{\partial x_j}}_{A_e} \underbrace{-\overline{\widetilde{u}'_i\widetilde{u}'_j}\frac{\partial \overline{\widetilde{u}}_i}{\partial x_j}}_{P} \underbrace{-\frac{\partial \overline{\widetilde{p}^{*\prime}\widetilde{u}'_j}}{\partial x_j}}_{\Pi_e} \\ & \underbrace{-\frac{\partial \overline{\widetilde{u}'_j e}}{\partial x_j} - \frac{\partial \overline{\widetilde{u}'_i\tau'_{ij}}}{\partial x_j}}_{T_e} + \underbrace{\overline{F'_i\widetilde{u}'_i}}_{-\epsilon_c} + \underbrace{\overline{\tau'_{ij}\widetilde{S}'_{ij}}}_{-\epsilon} \end{aligned} \tag{2}$$

Here, τ_{ij} is the subgrid scale stress tensor, $F_i = -C_d a\mathbf{P}|\widetilde{\mathbf{u}}|\widetilde{u}_i$ is the modeled canopy drag, $\widetilde{S}_{ij}$ is the resolved strain rate tensor, and $\widetilde{p}^* = (\widetilde{p}/\rho_0 + \tau_{kk}/3)$ is a modified pressure. In the expression for the canopy drag, C_d is a drag coefficient, $a(z)$ is the leaf area density, and $\mathbf{P}$ is a projection tensor (Pan et al. 2014). The terms on the right hand side are mean advection (A_e), shear production (P), pressure transport (Π_e), turbulent transport (T_e), canopy dissipation (ϵ_c) and SGS dissipation (ϵ). Note that the SGS transport term is lumped together with the turbulent transport.

Following Chamecki et al. (2018), we use the reduced TKE budget in which all terms that cause a local imbalance between production and dissipation of TKE are lumped into a residual term (R):

$$P - (\epsilon_c + \epsilon) = R = -A_e - \Pi_e - T_e. \quad (3)$$

All simulations analyzed here are in approximate steady state, justifying the assumption $\partial \overline{e}/\partial t = 0$ adopted above. The reduced TKE budget is then normalized by the total dissipation ($\epsilon_t = \epsilon_c + \epsilon$)

$$(P/\epsilon_t) - 1 = (R/\epsilon_t). \quad (4)$$

The ratio R/ϵ_t can be used to diagnose the local TKE budget: $R/\epsilon_t = 0$ represents a state of local balance between production and dissipation of TKE, while positive (negative) values of R/ϵ_t are associated with regions in which production is larger (smaller) than dissipation. Thus, we refer to R as the local imbalance term.

In the analysis of LES data, ensemble averages were replaced by time averages, and fluctuations were defined with respect to these averages. For the flat simulation, the ensemble average operation is replaced by time and horizontal averaging. In some analysis for the non-flat topography, turbulence statistics were averaged over terrain-following surfaces (i.e., surfaces of constant height above the topography, denoted by Z; see Appendix A), and this is represented by angle brackets. All the terms on the TKE budget (2) are independent of the frame of reference adopted and for simplicity data analysis was performed in the original cartesian coordinate system.

e. Application to tower measurements

Most tower observations in complex terrain are sited on the top of hills and ridges. To test some of the assumptions usually employed in interpretation of tower measurements and to provide more context to interpret these observations, we analyze in detail TKE budgets for virtual towers in the simulations. For the idealized topography, these are placed on the crest and trough of the topography. For the real topography, we chose 2 crests and 1 trough: "real ridge crest" is one of the highest crests in the domain and it is located on a fairly long 2D ridge; "real hill crest" is the highest point of a fairly isolated 3D hill; "real trough" is the lowest point in the entire domain (their locations are shown in Fig. 1). In addition, we also present some ensemble statistics for all crests and troughs in the domain, to illustrate the variability present in the real topography case. Note that for the purpose of this statistical analysis, we define crests and troughs based on the topographic variations along the mean wind direction as explained in the Supplement (the supplement also includes a figure with the location of all points considered as crests and troughs for this analysis).

In tower observations, only a few terms of the TKE budget can be estimated. Assuming a typical setup with turbulence measurements at multiple heights on a single tower, most of the terms that cannot be measured are negligible under the assumption of horizontal homogeneity. However, despite the small amplitudes of the topography, the flow field is strongly non-homogeneous and these assumptions may no longer be applicable. To facilitate interpretation of simulation results in the context of tower measurements, we follow Chamecki et al. (2020) and further break the local imbalance term R into a vertical component (R_v) consistent with the hypothesis of horizontal homogeneity and a horizontal component (R_h) characterized by deviations from that state

$$R = R^h + R^v, \tag{5}$$

with

$$R^h = -T_e^h - \Pi_e^h - A_e^h \tag{6}$$

$$R^v = -T_e^v - \Pi_e^v - A_e^v. \tag{7}$$

Here only the vertical transport term T_e^v is usually obtained from measurements and the vertical advection A_e^v can be calculated from observations but it contains large uncertainty (e.g., as illustrated by observational estimates of vertical advection of CO2 (Aubinet et al. 2003)) and it is usually neglected under the assumption of horizontal homogeneity (Chamecki et al. 2020). Note that this separation between horizontal and vertical components introduces a dependence on the choice of coordinate system. However, as we only apply this decomposition to troughs and crests, the cartesian coordinated system used in the simulation and the terrain-following coordinate system coincide, and deviations from the streamline coordinate system should be small. Thus, at these locations, there is no advantage in choosing a specific coordinate system and we use cartesian coordinates. The definitions used to separate the TKE budget terms into vertical and horizontal components are presented in the Appendix.

3. Results

a. TKE budgets

Our focus is mostly on the TKE budget within the canopy roughness sublayer, which is defined as $Z/h_c \leq 2$ and marked by the upper dashed line in most figures. The simulation of forest over flat topography (shown in the thin sub-panels in Figs. 2, 4, and 5 and as profiles in Fig. 6a) conforms to current knowledge derived from observations (Brunet et al. 1994) and LES (Dwyer et al. 1997; Chamecki et al. 2020). Shear production peaks at canopy top, decaying more quickly inside the canopy than above (Figs. 2a). Viscous dissipation follows a similar pattern, but it is much smaller than production near the canopy top (Fig. 2b). Inside the canopy, most of the sink of TKE is in the canopy dissipation, which is very large near the canopy top and decays towards the ground (Fig. 2c). The behavior of shear production and the two dissipation terms leads to a residual ($R = P - \epsilon_t$) that is positive above the canopy and mostly negative within the canopy, leading to the strong vertical transport of the excess TKE produced above the canopy to balance the excess dissipation within the canopy (Figs. 2d and 4a). For practical purposes, the flow can be divided into three distinct layers: the lower canopy where most of the imbalance is caused by pressure transport ($R \approx -\Pi$), the upper canopy and the roughness sublayer where most of the imbalance is caused by turbulent transport ($R \approx -T_e$), and the inertial layer above (roughly at $Z/h_c > 2$), where the imbalance is approximately zero so that $P \approx \epsilon$ (i.e., the layer where the law-of-the wall applies).

Comparison of the main terms in the TKE budget between the flat and the idealized topography cases in Figure 2 shows strong modulation of shear production and dissipation by the topography. The shear production displays strong inhomogeneity in the along topography direction, with enhanced production located around the crests of the topography in the upper canopy and in the lower part of the roughness sublayer (coincident with regions of increased shear due to the flow speedup above the crests). This inhomogeneity persists across the roughness sublayer and above, except that the horizontal position of the peak is displaced downwind from its location at the canopy top. The viscous dissipation is much closer to being homogeneous, with some deviations in the roughness sublayer that quickly disappear higher up. The canopy dissipation is strongly inhomogeneous in the upper canopy, with larger dissipation in the upwind portion of the ridges where velocities within the canopy are larger. These patterns lead to a local imbalance R that is nearly homogeneous inside the canopy, with strong deviations from homogeneity above the canopy. This inhomogeneity weakens (but does not disappear) above the roughness sublayer. Note that strong deviations from horizontal homogeneity driven by shear production persist at least up to $z = 200\,\mathrm{m}$ (this is more clearly seen in Figure 4), preventing a local balance between production and dissipation to be established and, consequently, precluding the formation of an inertial sublayer as suggested by Chamecki et al. (2020).

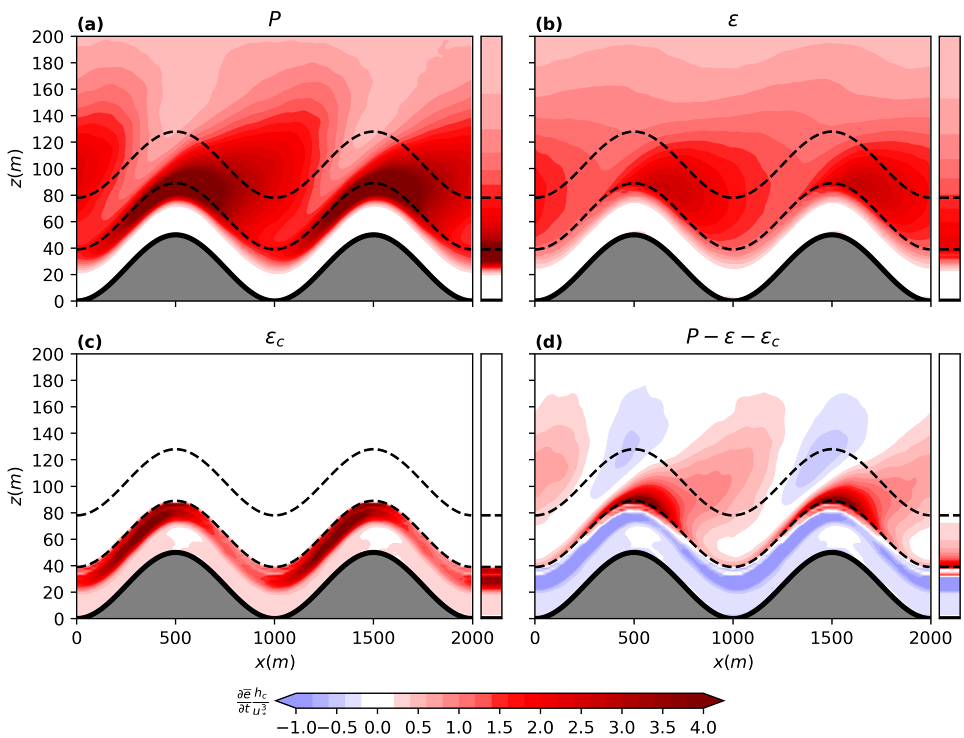

FIG. 2. TKE production and dissipation terms for the simulation with idealized topography. Results for flat topography are also shown as small lateral panels for comparison. Note that we use $\partial\overline{e}/\partial t$ in the caption to refer generically to the terms on the right-hand side of Equation 2.

Before proceeding with the analysis, we note that in the cases with topography some of the flow mean kinetic energy is dissipated by the pressure force on the ground surface (i.e. the dissipation caused by the form drag associated with the topography). Because the forcing is constant across all simulations, the topography drag leads to slightly smaller rates of production and dissipation of TKE within the flow as indicated by the total (volume integrated) TKE production and dissipation (Table 2). As expected, the reduction in total dissipation is proportional to that in total shear production,

TABLE 2. Total (volume integrated) production and dissipation for each simulation. The quantities are normalized by the equivalent friction velocity u_*.

Quantity	"Flat"	"Idealized"	"Real"
$\int P \mathrm{d}V / (u_*^3 L_x L_y)$	7.51	7.39	6.95
$\int \epsilon_t \mathrm{d}V / (u_*^3 L_x L_y)$	7.68	7.43	7.21
$\int (P - \epsilon_t)\, \mathrm{d}V / (u_*^3 L_x L_y)$	-0.17	-0.04	-0.26
$\int \frac{\partial \overline{e}}{\partial t} \mathrm{d}V / (u_*^3 L_x L_y)$	-0.02	-0.02	-0.01

such that the balance between total production and total dissipation in the domain is approximately maintained for each flow. The average rate of change of TKE is very small in comparison to shear production and dissipation (always smaller than 0.3%), supporting the assumption of stationary turbulence. The net budget of total production and dissipation is slightly larger than the time change in TKE, and this difference is attributed to the small errors incurred in the interpolations required in the post-processing of the LES results. More importantly, the reduction in production and dissipation are not uniformly distributed in the vertical, being significantly stronger in the upper canopy (see Figure 3). Note that because the total dissipation varies in space, this is not a traditional normalization in which the magnitudes are modified but the spatial patterns of the variables are preserved. Rather, this is a direct comparison of each term in the TKE budget to the local rate of dissipation.

Instead of adopting the usual normalizations of the TKE budget terms for canopy flows using h_c/u_*^3 (Raupach and Thom 1981; Finnigan 2000) employed in Figures 2 and 3, for the remaining of this analysis we follow the reduced TKE approach of Chamecki et al. (2018) and normalize all terms by the total local rate of dissipation ϵ_t. On one hand, this normalization accounts for the small difference in total production and dissipation between flat and non-flat topographies (and its vertical distribution). More importantly, it allows us to interpret all the terms of the TKE budget based on how much they contribute to the total local dissipation, which is especially useful in the lower canopy where all terms are very small compared to their values in the upper canopy.

The normalized residual R/ϵ_t and its partition into advection, turbulent transport, and pressure transport (see Equation 3) for the idealized topography case are shown in Figure 4. The same 3-layer structure from flat topography is still discernible in this more complex case. In the lower canopy imbalance is still caused mostly by pressure transport, and no significant deviations from "horizontal" homogeneity are noticeable. In the upper canopy and the lowest portion of

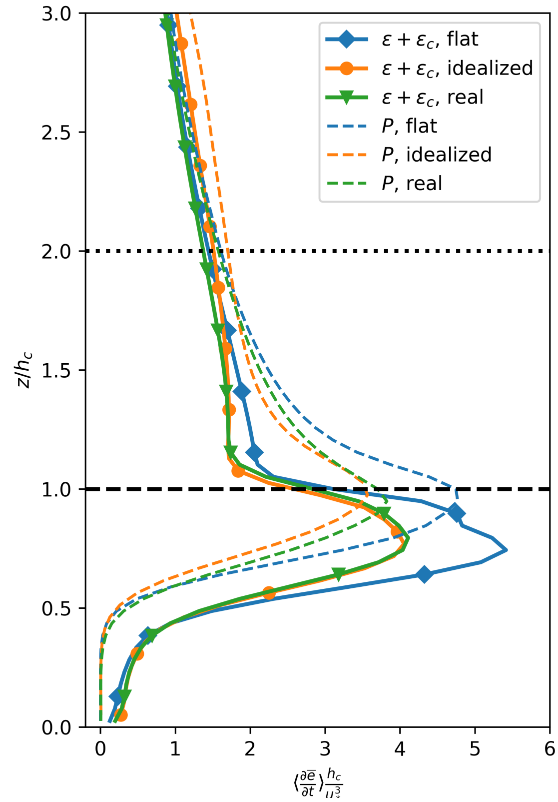

FIG. 3. "Horizontally" averaged shear production and TKE dissipation rate profiles for all 3 simulations.

the roughness sublayer above the canopy, most of the imbalance is due to turbulent transport, and while some deviations from "horizontal" homogeneity are noticeable, these are still not dominant. This layer is shallower than in the flat terrain case, because advection and pressure effects introduced by the topography become very important roughly in the middle of the roughness sublayer ($Z/h_c \approx 1.5$). This layer extending from the ground up to about $Z/h_c \approx 1.5$ can be considered analogous to the inner layer of neutral flow over a rough and gentle isolated hill (Belcher et al. 1993; Kaimal and Finnigan 1994), even though noticeable deviations from "horizontal" homogeneity are already present. Above this inner layer, the residual oscillates between positive and negative bands that result from the complex patterns of the transport terms (mostly advection and turbulence transport).

The partition of the residual is shown in the Supplement for the simulations "Half" and "Double". General patterns are very similar to those seen in Figure 4, except that increasing the hill height increases the modulation of the residual by the topography and the contrasts between positive and

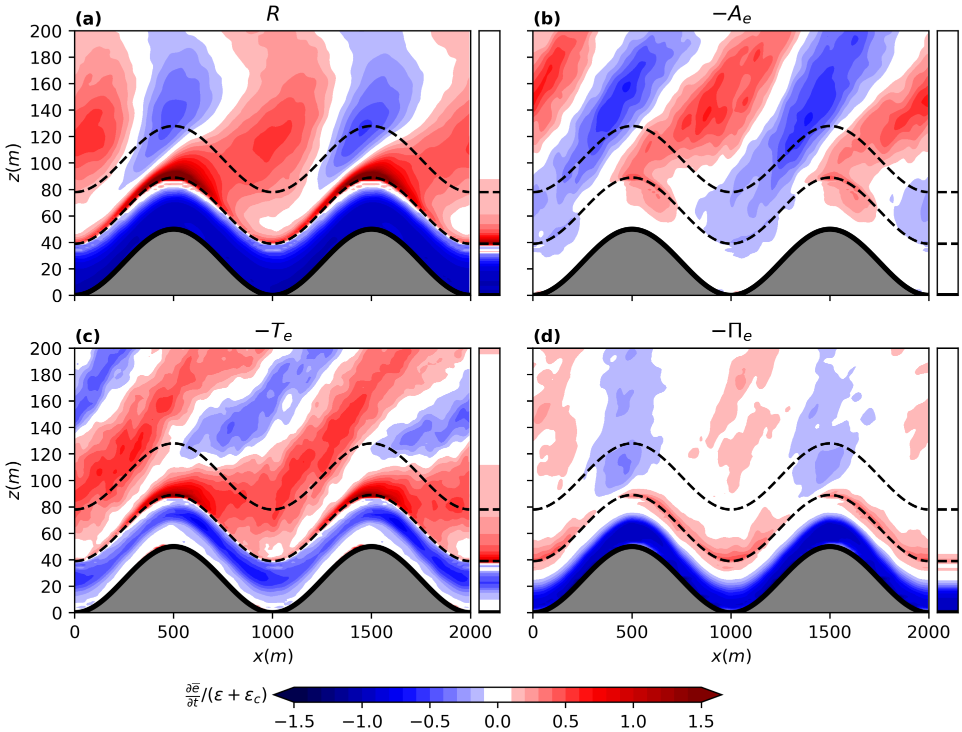

FIG. 4. TKE residual and its main contribution from different transport terms for the simulation with idealized topography. Results for flat topography are also shown as small lateral panels for comparison.

negative regions. Perhaps the one relevant conclusion from the comparison is that the region of negative residual $R < 0$ within the roughness sublayer above the crests becomes more clear as the slope of the topography increases. In addition, pressure transport becomes more important for the "Double" case with slope $H/L = 0.4$.

The same analysis is repeated for two cross-sections (one in the mean wind direction and one in the cross-wind direction, as indicated in Figure 1) of the real topography in Figure 5. The level of complexity in the real topography is significantly enhanced compared to the idealized topography, and deviations from "horizontal" homogeneity are clearly seen in the entire vertical extent of the flow (note that the domain is much higher than the portion shown in the figures). The 3-layer structure is much less clear than in the flat and idealized topography cases. Effects of turbulent transport extend into the lower canopy downstream of crests, but due to the uneven spacing between topographic features, this enhanced turbulent transport sometimes interacts with the windward face of the downstream ridge (e.g., see small ridge at $x = 1800\,\text{m}$ in Figure 5e).

Similarly, mean advection effects are strong within the entire roughness sublayer and even inside the canopy. The interaction of shear layers from one crest with downwind features leads to a less organized pattern, which in the present case seems to extend farther from the ground (note that strong inhomogeneity is still clear at $z = 200\,\mathrm{m}$). The patterns of the terms in the TKE budget are more strongly determined by the upstream topography in the mean wind direction (as opposed to the cross-wind direction), but general conclusions are difficult.

Chamecki et al. (2020) used the existence of a region above the canopy in which production is smaller than dissipation (resulting in $R < 0$) to identify the effects of topography in tower data. This feature is clearly present in the idealized topography (see Figure 4a). In the real topography, similar regions can be identified over some of the crests (e.g., see the small crest at $x \approx 600\,\mathrm{m}$ and the tall crest at $x \approx 2300\,\mathrm{m}$ in Figure 5a). However, other large crests do not display this feature (e.g. the large crest at $x \approx 1400\,\mathrm{m}$ in Figure 5a). This difference in behavior seems to be caused mostly by the advective transport that has strong negative contributions in cases were $R < 0$ is observed but not on the large crest in which R remains positive. Therefore, even though regions of $R < 0$ can be used to identify effects of topography on the TKE budget above crests, not all crests display this feature and the absence of such a region cannot be used to infer that effects of topography are negligible.

An important practical question is whether the presence of gentle topography alters the TKE budget in a fundamental way or if it only creates “horizontal” variability. We investigate this by performing “horizontal” averages over the entire simulation domain. Clearly, the advection term is negligible at all heights and in all cases after “horizontal” averaging. Given the profiles of production and dissipation shown in Figure 3, we would expect the “horizontally” averaged budgets to be impacted by topography. However, when the average profiles are normalized by the averaged dissipation profile $\langle \epsilon_t \rangle(Z)$, the TKE budget terms for all three simulations are very similar (see Figure 6; a similar figure using the more traditional normalization is included in the Supplement for completeness). The most significant difference between the 3 cases is the partitioning of the dissipation in the lower canopy, which has more contribution from viscous dissipation and less from canopy drag in the topography cases (suggesting slightly higher levels of turbulence inside the canopy). The most important conclusion from this analysis is that the approximate balance between production and dissipation (indicated by $\langle P \rangle / \langle \epsilon_t \rangle \approx 1$ above $Z/h_c = 2$ in all 3 panels) that

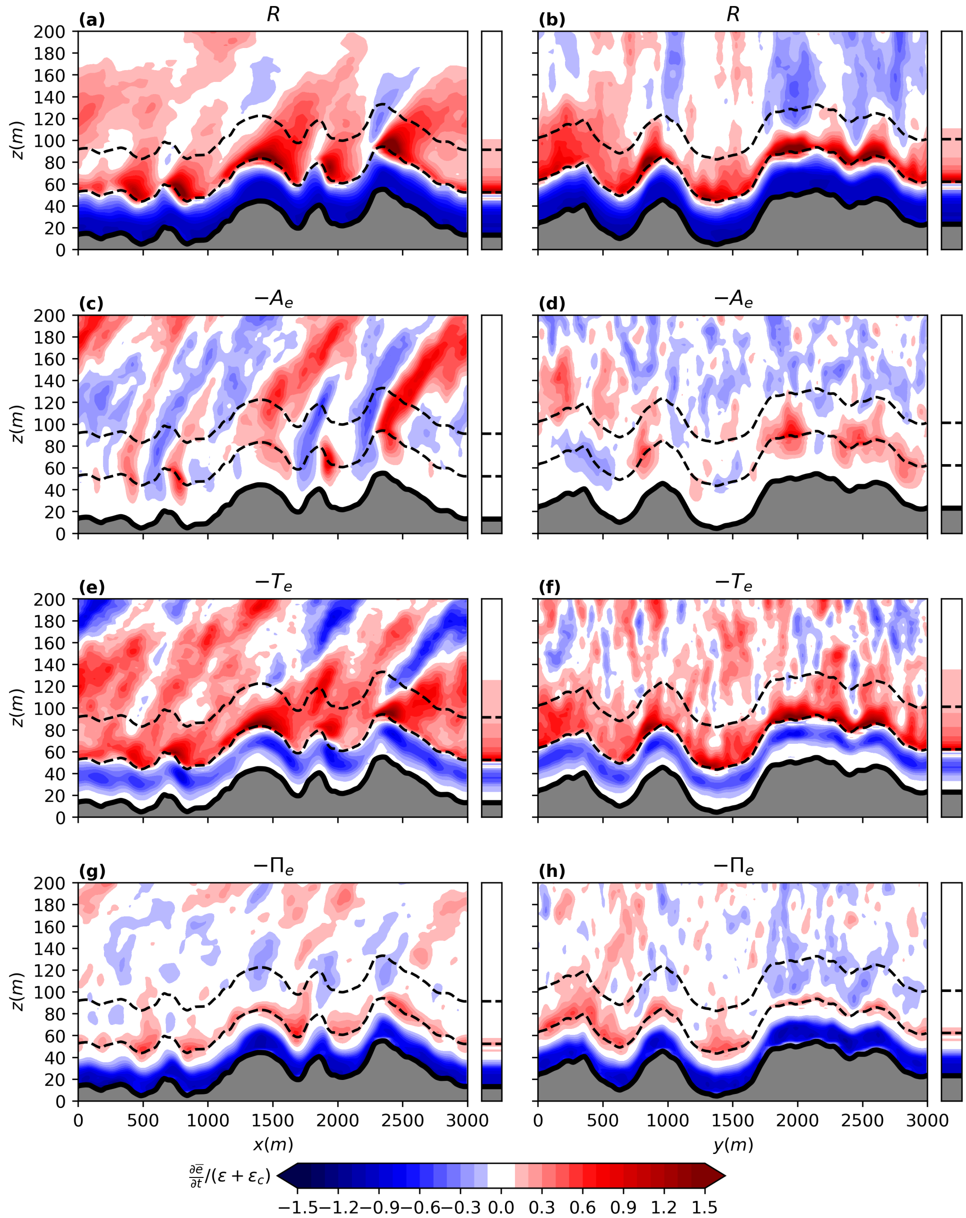

FIG. 5. TKE residual and its main contribution from different transport terms for the simulation with real topography: (a) downstream cross-section at y =1500 m and (b) crosswind cross-section at x =917.5 m. Results for flat topography are also shown as small lateral panels for comparison.

characterizes the inertial sublayer above the roughness sublayer is recovered upon "horizontal" averaging over gentle topography.

Two remarks are important in the interpretation of Figure 6. Results presented here are valid for gentle topography, and similar analysis applied to the "Double" case shows that turbulent transport

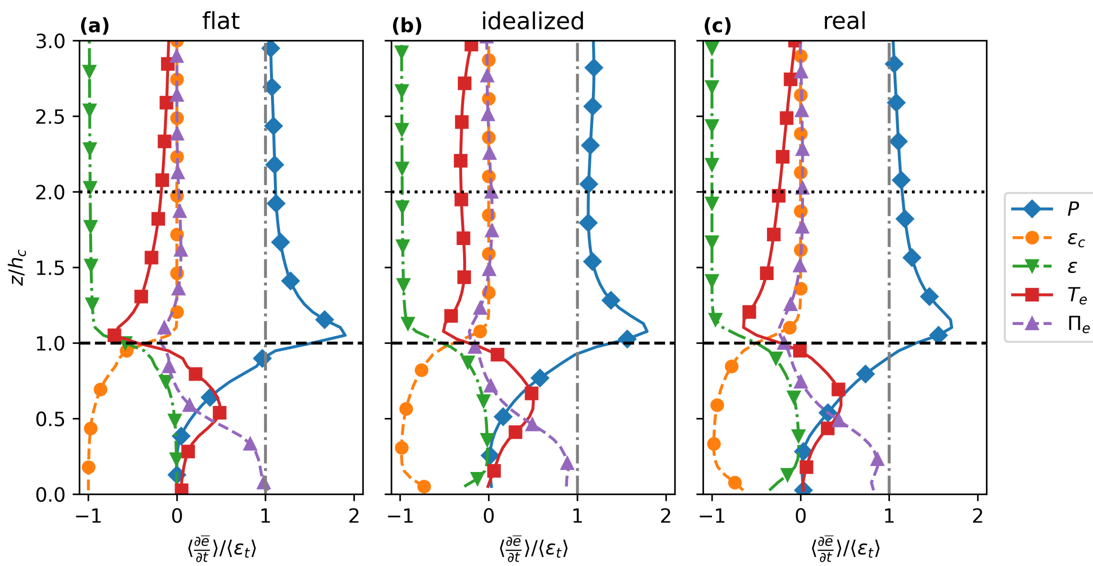

FIG. 6. "Horizontally" averaged profiles of TKE budget terms for (a) flat, (b) idealized, and (c) real topography. Terms are normalized by total dissipation rate (sum of the dissipation rate and the canopy drag work).

and advection are significantly different from the flat case even after "horizontal" averaging (not shown), precluding the existence of an inertial sublayer even in average sense. Finally, the nearly perfect agreement between the 3 panels in Figure 6 is, in part, caused by the fact that there is nearly perfect cancelation between topographic features in the periodic domain. If a similar analysis is carried out in a patch of real topography (without periodic boundary conditions), one would expect that the spatial averaging would strongly reduce the effects of topography on the TKE budget, converging to the flat terrain case as the number of topographic features contained in the patch becomes very large.

b. Virtual towers

The analysis of virtual towers has two main goals: (i) explore the processes that are relevant for the TKE budget at topography crests and troughs where towers are usually sited, and (ii) guide the interpretation of field observations. Because the former is better accomplished by presenting profiles normalized by dissipation, we choose to present those in the main manuscript. However, we recognize that estimates of the TKE dissipation rates from measurements is difficult (especially inside the canopy), and complementary figures using the standard normalization for TKE budget terms in canopy flows (using h_c/u_*^3) are provided in the Supplement.

The main terms of the TKE budget at the virtual towers are shown in Figure 7, where the flat case is also shown for comparison (see also Figure 2 in the Supplement). In general, there are important differences between crests, troughs, and flat terrain. The peak in production just above the canopy is very large at the crests, and the faster decay in production with height above this peak leads to regions in which production is smaller than dissipation ($R < 0$, which corresponds to regions in which $P/\langle\epsilon_t\rangle < 1$ in the figure). The crossing to $P/\langle\epsilon_t\rangle < 1$ occurs approximately at $Z/h_c = 1.5$ (for some smaller crests in the real topography, this crossing is located higher up and sometimes it is not as clear). The troughs show a double peak in production above the canopy, with production (almost) always larger than dissipation. The upper peak in production is associated with the shear layer from the upstream crest, and most of the energy excess in this region is removed by turbulent transport (contrary to flat terrain and crests, the vertical transport by turbulence remains large above the roughness sublayer due to the elevated shear layers). As discussed before, inside the canopy the differences from the flat case are less pronounced. In the upper part of the canopy, advection can still play an important role, being mostly negative over crests and positive over troughs.

A more complete analysis of the contributions of different terms to the residual is shown in Figure 8. In this figure, all positive (negative) terms (except R) indicate an energy loss (gain). The horizontal transport by pressure and turbulence (not shown) are negligible at all heights in the profiles shown in Figure 8, and whenever R^h is important in the budget one can safely assume that it is dominated by horizontal advection (i.e., $R^h \approx -A_e^h$). The simplicity of the residual for the flat case, transitioning from being almost entirely caused by vertical turbulent transport in the upper canopy and above to being almost entirely caused by pressure in the lower canopy no longer holds in the cases with topography. While the presence of horizontal advection was expected, the importance of vertical advection at crests and troughs is quite remarkable. Over the crests, mean vertical advection of TKE transports energy upwards, acting as a sink in the upper canopy region and as a source for $Z/h_c > 1.5$. The opposite is seen over the troughs, where this mean vertical advection is a source of TKE in the entire vertical extension of the roughness sublayer. These effects can be easily explained by the gradients in mean vertical velocity and TKE (shown in the Supplement). This is especially true above the canopy, where the vertical gradients in TKE are fairly small and the advection is mostly determined by the gradients in $\overline{w}$. However, there is large cancellation between horizontal and vertical mean advection in the cartesian coordinate system

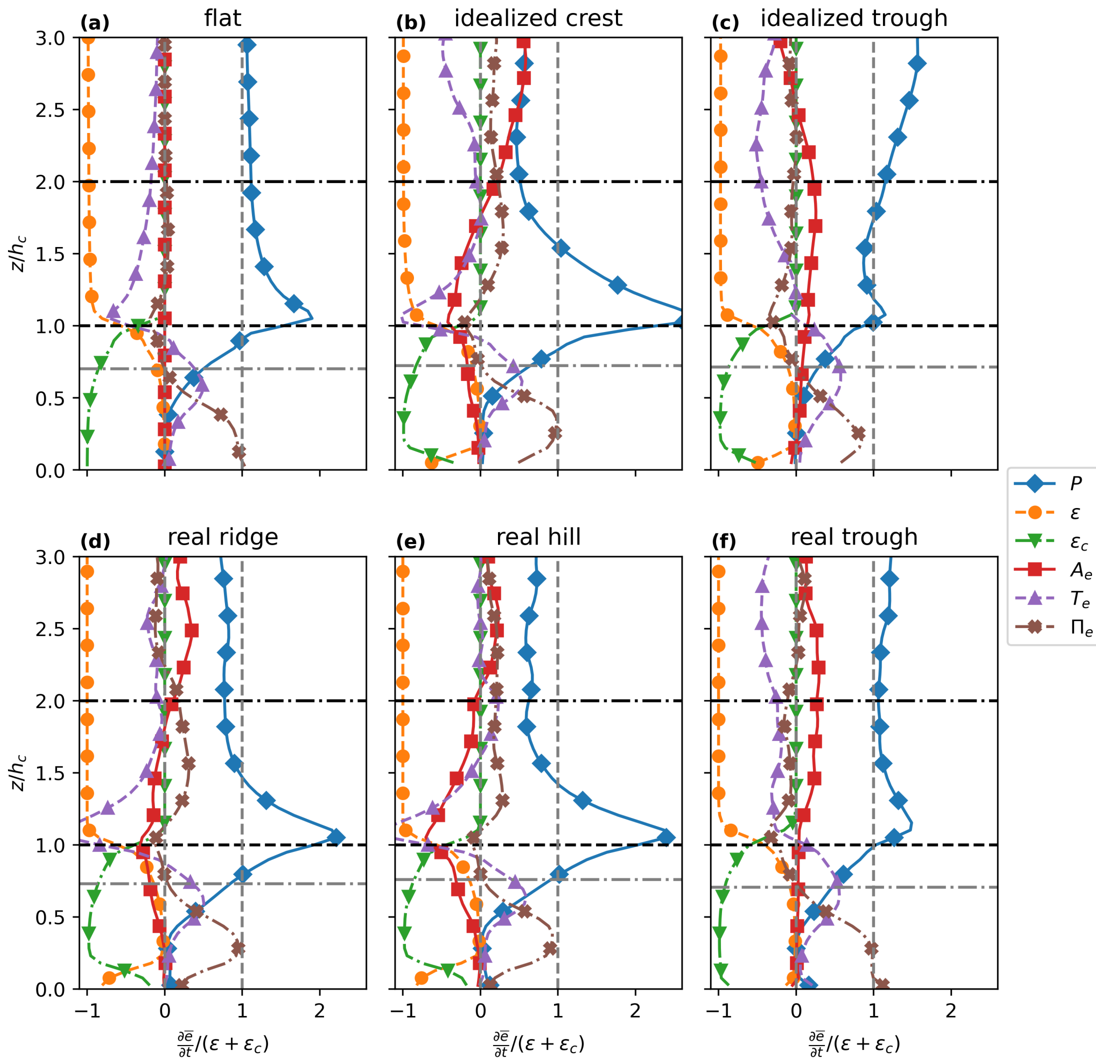

FIG. 7. Profiles of TKE budget terms normalized by the local dissipation at selected virtual tower locations: (a) flat, (b) idealized crest, (c) idealized trough, (d) real ridge, (e) real hill, and (f) real trough. The locations of virtual towers for the real topography can be viewed in Figure 1. The grey dot-dashed line indicates the displacement height, calculated following Jackson (1981).

adopted (something that would be eliminated in the streamline coordinate system). For the real topography, the patterns of horizontal and vertical transport by mean advection vary significantly in space (not shown), as they depend strongly on the position of the shear layers and the flow field patterns upwind. Interestingly, the contributions of pressure transport are practically negligible, except in the lower canopy. From an observational perspective this is very important, since pressure fluctuations are rarely measured in field campaigns.

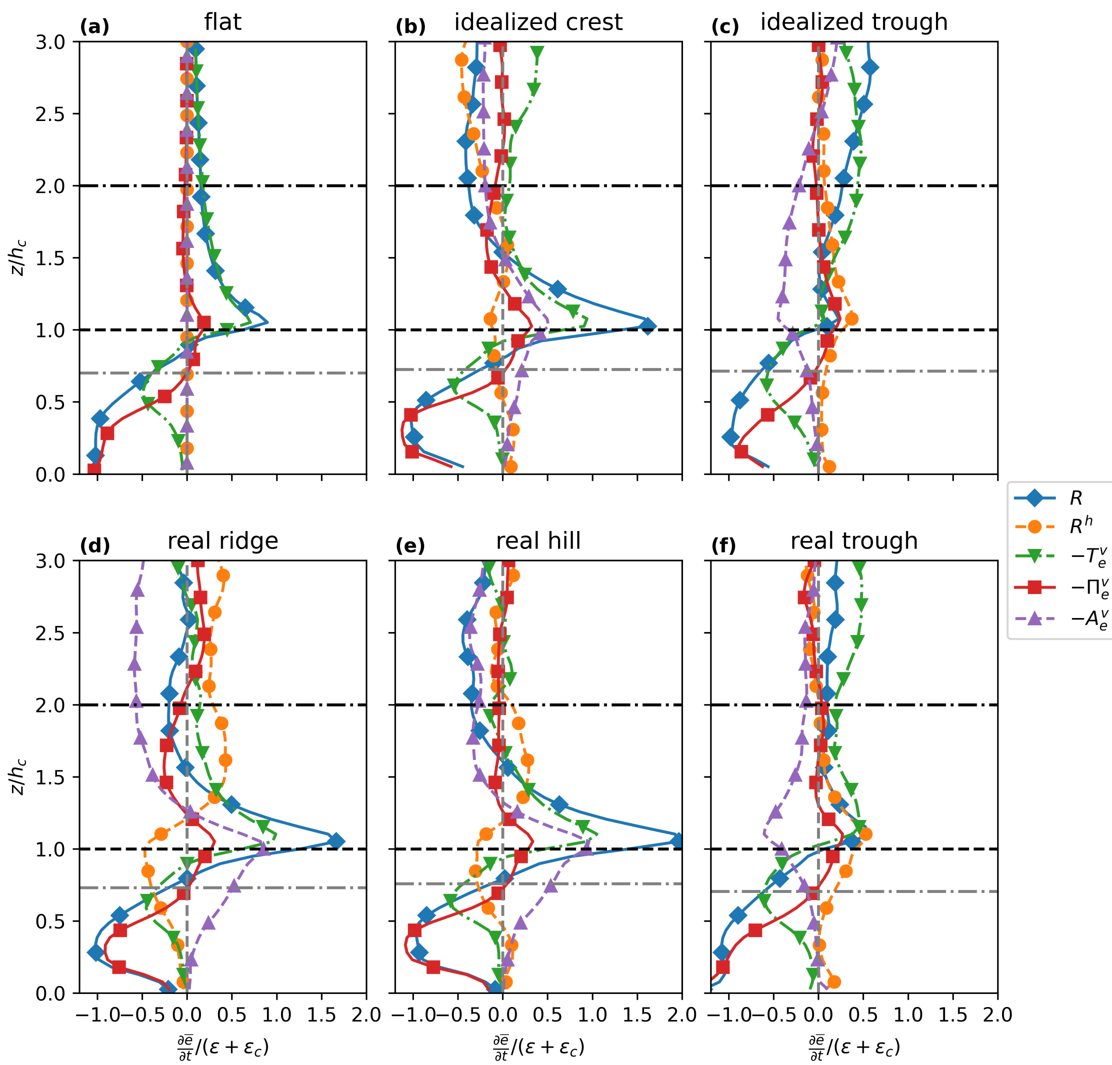

FIG. 8. Profiles of TKE residual R and its partition into individual vertical transport terms and a lumped horizontal term representing deviations from horizontal homogeneity for the same virtual tower shown in Figure 7. Note that Eqns. (5)-(7) imply $R = R^h - T_e^v - \Pi_e^v - A_e^v$.

In order to characterize the impact of topography on the TKE budget we note that, in flat terrain we have $R = -T_e^v - \Pi_e^v$ (see Figure 8a). Our results also show that horizontal transport by turbulence and pressure fluctuations are negligible at the topography crests and troughs ($T_e^h/\epsilon_t \approx 0$ and $\Pi_e^h/\epsilon_t \approx 0$). Therefore, most of the distortions introduced by topography ate crests and troughs are expressed in the TKE budget via horizontal and vertical advection. Motivated by this observation, we use the advection term normalized by the total dissipation as an "advection index"

$$\mathcal{I}_A = \frac{|A_e|}{\epsilon_t}. \tag{8}$$

$\mathcal{I}_A$ quantifies the importance of advection in terms of the local rate of dissipation, and it serves as a proxy for the impact of topography on the local TKE budget. Clearly the advection term is identically zero flat topography ($A_e = 0$) so that $\mathcal{I}_A = 0$. Deviations from zero are indicative of topography effects (or other source of non-homogeneity), and larger values of $\mathcal{I}_A$ are associated with larger effects of topography on the local TKE budget. Profiles of $\mathcal{I}_A(z)$ are shown in Figure 9. The lower canopy is characterized by $\mathcal{I}_A < 0.05$, implying minor effects of topography on the TKE budget as inferred from the previous discussions. Values increase in the upper canopy reaching values typically between 0.1 and 0.7 and peaking just above the canopy. Values of I_A are larger over crests than over troughs. In general, the effects of topography present a slow decay with height within the roughness sublayer (in some cases secondary peaks are present), but are still significant at $Z/h_c = 3$. For the 3 ideal cases (labeled "Half", "Idealized", and "Double" in Figure 9), the behavior of $\mathcal{I}_A$ changes systematically indicating stronger effects of advection with increasing topography slope over the crests: both the peak value of I_A near the canopy top and the the values at the secondary peak above $Z/h_c = 2$ increase with increasing slope. Note that the height of the minimum I_A between these two peaks decreases with increasing slope. All these features are also present in the real topography cases. However, over the trough, the effects of advection increase from "Half" to the "Idealized" case as expected, but the "Double" case has a very different behavior. This is caused by the fact that in the "Double" case the slope is large enough that the recirculation region in the lee of the hill extends far above the canopy, while in the other two cases the recirculation bubble is completely contained inside the canopy (this can be clearly seen in Figure 3 of Chen et al. (2019). The larger recirculation changes the nature of advection over the trough, reducing the mean velocities and increasing the turbulence intensity (and thus the rate of dissipation) in this region, and leading to a reduction in the values of $\mathcal{I}_A$ when compared to the gentler topography cases. Based on the theory of Finnigan and Belcher (2004) and the numerical simulation of Ross and Vosper (2005), we expect that increasing the canopy density or reducing the hill length (while maintaining the same slope) will increase the mean advection across the canopy top and lead to similar results as those resulting from an increase in slope.

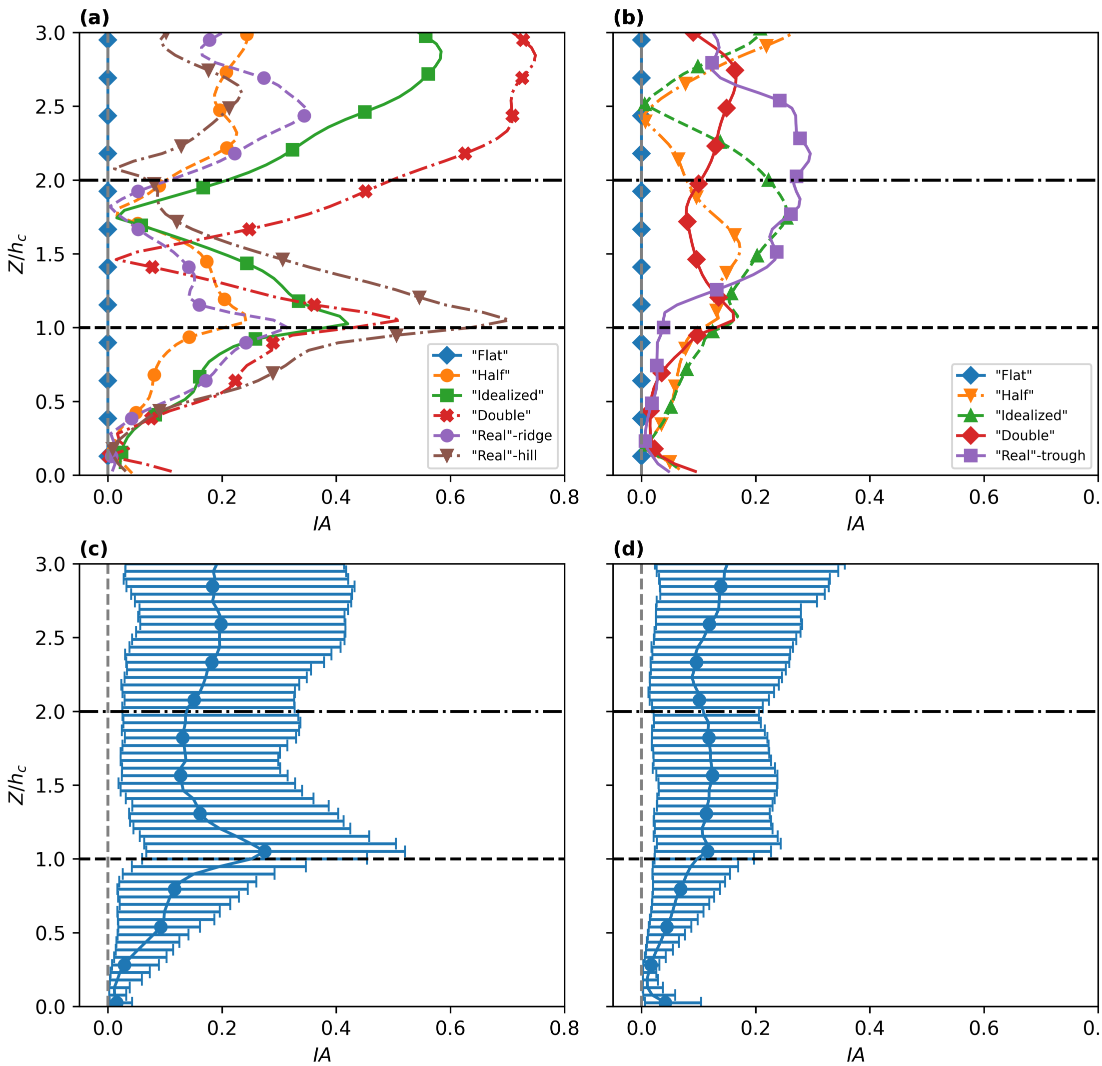

FIG. 9. Profiles of the topography index $\mathcal{I}_A$ for selected virtual towers on (a) crests and (b) troughs, and median and 10% and 90% percentiles for (c) all crests and (d) all troughs.

To describe better the "Real" case, we also present median values and 10% and 90% percentiles for all crests and troughs as a measure of the range within which most points are contained (Figures 9c,d). Despite the fairly large variability of $\mathcal{I}_A$ over crests and troughs within the domain, one could choose $\mathcal{I}_A \geq 0.1$ as a reference value indicating regions in which the contribution from the advection term is more than 10% of the local dissipation, and so topographic effects become relevant.

Finally we look into the approximations that are usually employed in tower observations. First, shear production is usually estimated based on the homogeneous definition valid for flat terrain

$$P_{homo} = -\overline{u'w'}\frac{\partial \overline{u}}{\partial z}. \tag{9}$$

For most of the virtual towers in our simulations this is a reasonable approximation. In the worst case from the selected virtual towers (real ridge), this approximation leads to an underestimation of the peak in production of at most 20–25%, being quite accurate away from the peak (see Figure 5 in the Supplement). Pressure terms are usually neglected, and this is a very good assumption in the upper canopy and above. Chamecki et al. (2020) estimated the residual from $R = P - \epsilon$ and then, assuming vertical advection to be negligible, estimated horizontal advection from the residual as $A_e^h = R - T_e^v$ (only above the canopy). Clearly vertical advection is not negligible, and even though it can be estimated from tower measurements, this is far from trivial. The LES results presented here suggest the best approach for single tower measurements is to estimate the residual from $R = P - \epsilon_t$, and then use the residuals to estimate total advection in the upper canopy and above and pressure transport in the lower canopy. Thus, we have

$$A_e \approx -(R + T_e^v) \quad \text{(upper canopy and above)} \tag{10}$$

$$\Pi_e^v \approx -(R + T_e^v) \quad \text{(lower canopy).} \tag{11}$$

The applicability of these two approximations is assessed for all crests and troughs in Figure 10, and correlation coefficients and root mean squared errors (RMSE) are presented in Table 3. Note that in all estimates the terms are normalized by the total dissipation. For practical purposes, we define the separation between lower and upper canopy at $Z/h_c = 2/3$, and show results in the range $0 \leq Z/h_c \leq 2$.

The approximation given by Equation (10) is excellent above the crests, but fairly poor over the troughs, implying that the role of horizontal transport by turbulence and/or the pressure transport are still important for the latter. From the observational perspective of estimating the TKE budget and the advection index above the canopy for towers usually sited on the crests of the topography,

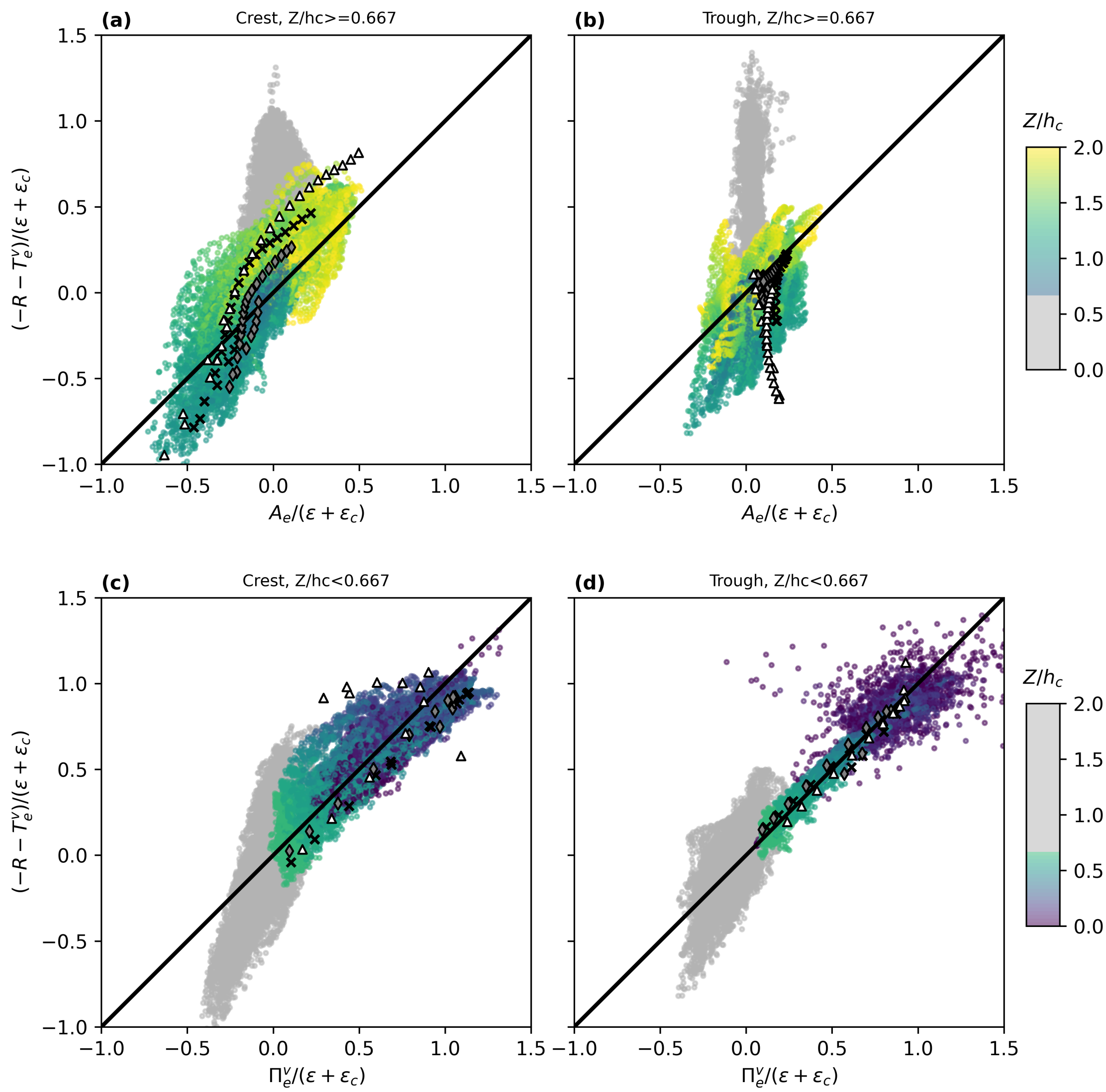

FIG. 10. Estimates of (a,c) horizontal advection using Equation (10) and (b,d) horizontal pressure transport using Equation (11) for real topography (colored dots) and ideal topography (crosses, diamonds, and triangles indicate cases "Idealized", "Half", and "Double", respectively). Grey dots are used for real topography points outside the range of height in which the relationships are expected to be valid (for idealized topography these points are not shown). Panels (a,b) are for all crests and (c,d) for all troughs in the real topography.

Equation (10) yields high correlation coefficients (always larger than $r = 0.8$) and moderate RMSEs (always smaller than 0.3). The RMSE for the Real case suggests a typical error in the estimate of A_e/ϵ_t around 0.2. For the three ideal cases, even though the correlation coefficients increase with increasing topography height (and consequently increasing slope), the RMSE also increases suggesting that the approximation becomes less accurate for increasing slopes. As expected, the role of the pressure transport increases with increasing slope.

The deep-canopy approximation given by Equation (11) is much more accurate than Equation (10), being more accurate over troughs. For the ideal cases, while the RMSE increases with increasing slope over the crests, it remains small and nearly constant over the troughs. These results suggest that for the dense canopy studied here, advection starts impacting the deep-canopy flow at the crests for slopes larger than 0.2. Advection is still negligible at the troughs for slopes as large as 0.4.

Location	Z/h_c	Eq.	variable	r	RMSE
Idealized crest	$\geq 2/3$	(10)	A_e/ϵ_t	0.93	0.23
Idealized trough	$\geq 2/3$	(10)	A_e/ϵ_t	0.56	0.16
Half crest	$\geq 2/3$	(10)	A_e/ϵ_t	0.89	0.15
Half trough	$\geq 2/3$	(10)	A_e/ϵ_t	0.39	0.11
Double crest	$\geq 2/3$	(10)	A_e/ϵ_t	0.97	0.30
Double trough	$\geq 2/3$	(10)	A_e/ϵ_t	-0.71	0.44
Real crests	$\geq 2/3$	(10)	A_e/ϵ_t	0.81	0.19
Real trough	$\geq 2/3$	(10)	A_e/ϵ_t	0.55	0.18
Idealized crest	$< 2/3$	(11)	Π_e^v/ϵ_t	1.00	0.16
Idealized trough	$< 2/3$	(11)	Π_e^v/ϵ_t	0.98	0.05
Half crest	$< 2/3$	(11)	Π_e^v/ϵ_t	1.00	0.13
Half trough	$< 2/3$	(11)	Π_e^v/ϵ_t	0.98	0.06
Double crest	$< 2/3$	(11)	Π_e^v/ϵ_t	0.43	0.34
Double trough	$< 2/3$	(11)	Π_e^v/ϵ_t	0.98	0.06
Real crests	$< 2/3$	(11)	Π_e^v/ϵ_t	0.88	0.15
Real trough	$< 2/3$	(11)	Π_e^v/ϵ_t	0.94	0.10

TABLE 3. Correlation coefficients (r) and root mean squared errors (RMSE) for estimates of A_e^h/ϵ_t and Π_e^v/ϵ_t from the TKE budget using equations (10) and (11).

Based on the results presented above, we outline a tentative procedure to estimate $\mathcal{I}_A$ above the canopy from single tower measurements:

1. Estimate shear production (P_{homo}), buoyancy production/destruction, and vertical turbulent transport of TKE;
2. Estimate dissipation using the spectrum or the second-order structure function for the streamwise velocity component;
3. Estimate mean total advection using Equation (10);

4. Calculate $\mathcal{I}_A$ using Equation (8).

4. Discussion and conclusions

In this study we employed LES to study the TKE budget within and above forests, contrasting flat terrain with gentle topography. While the TKE budget over idealized sinusoidal ridges is still fairly simple, the real topography is much more complex and general conclusions are not always possible. Nevertheless, some important observations can be highlighted here. First and foremost, our LES results agree with observations from the Amazon forest (Kruijt et al. 2000; Gerken et al. 2017; Santana et al. 2018) and theory (Finnigan and Belcher 2004) in the fact that no clear mean wind speed-up maxima is noticeable within (or slightly above) the roughness sublayer (see Figure 2(a) in the Supplement). However, observations (Chamecki et al. 2020) and our simulations presented here clearly show that the TKE budget is strongly impacted by the presence of the gentle topography. We conclude that the TKE budget may provide a better measure of the effects of topography than the mean wind speed profile in single tower observations.

Deviations from "horizontal" homogeneity in the TKE budget are fairly small within the lower canopy. In the upper canopy and above, these deviations become very large and are mostly caused by mean advection of TKE. "Horizontal" transport by pressure and turbulence are negligible for the gentle slopes studied here, while both horizontal and vertical advection are important. Vertical transport by pressure is also impacted by topography, being more important than over flat topography. The patterns in the TKE transport are such that, above crests in the topography, one usually has a region in which local production is smaller than local dissipation ($P < \epsilon \Rightarrow R < 0$, e.g., see Figure 8), with the sum of the transport terms acting as a sink. This is a unique feature not present in the canonical roughness sublayer or in the convective mixed layer above flat terrain, and can be used as one possible identifying feature of the effect of topography (or other sources of deviation from horizontal homogeneity) in single tower measurements. Nevertheless, despite these modifications, when the TKE budget is averaged over terrain-following surfaces, the flat terrain balance between production dissipation and vertical transport by turbulence is recovered, including the existence of an average inertial sublayer in which production is in approximate balance with dissipation above the roughness sublayer as is the case for flow over rough hills (Wood and Mason 1993) (therefore, for gentle topography, we expect the log-law and Monin-Obukhov similarity to be good approximations above the roughness sublayer after averaging over a large horizontal extension as done implicitly in large-scale models).

Production is not always smaller than dissipation above crests in complex terrain, so this feature is not a reliable proxy for the effects of topography on the TKE budget. Instead, we showed that most of the effects of the topography on the TKE budget above the canopy manifest via mean advection. Thus, we introduced an "advection index" (see Equation 8) as a way to assess topographic effects from single tower measurements. Estimating $\mathcal{I}_A$ from observations is not trivial (e.g., estimating the rate of dissipation accurately from tower measurements is quite challenging, and the approximation to estimate advection given by Equation 10 will introduce additional error), and the methodology proposed here must be tested with observational data in the near future.

Many questions remain, and further studies of the TKE budget over complex terrain covered by forests are needed. Even though our results are strictly valid for "horizontally" uniform forests, it is reasonable to expect that results will be similar for non-uniform forests as long as the spatial heterogeneity induced by the forest variation is small compared to that indued by the topography itself. If forest spatial structure becomes dominant, the mean TKE advection term will be dominated by changes in forest cover. Our general approach should still be valid, but deviations from the canonical flow over uniform forests over flat terrain will now be an indication of strong spatial structure in forest cover. Finally, results presented here are only valid for neutral atmospheric stability conditions and future steps should include the generalization of this study to other real topographies and non-neutral atmospheric stability.

Acknowledgments. This work was supported by the U.S. National Science Foundation (AGS-1644375) and by the Biological and Environmental Research (BER) program of the Department of Energy (DE-SC0022072).

Data availability statement. Data needed for reproducing the figures and tables are publicly available at https://zenodo.org/record/7065494 (doi:10.5281/zenodo.7065494). Please contact the corresponding author for additional information regarding the data set and numerical model.

APPENDIX A

IBM implementation

The topography is represented in LES using an immersed boundary method (IBM) slightly modified from Chester et al. (2007), which is based on the discrete forcing approach Mittal and Iaccarino (2005). The advantages of the IBM method are its simplicity and low computational cost to represent topography on a Cartesian grid (e.g., as opposed to the more accurate use of curvilinear coordinates). The current implementation is summarized below and the main components are also illustrated in Figure A1.

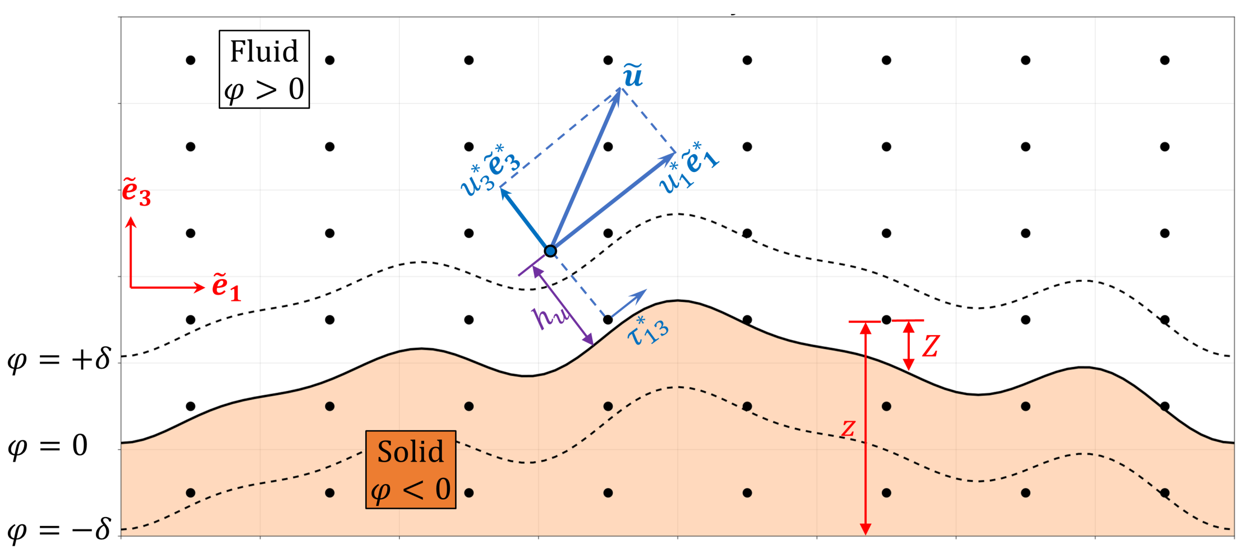

FIG. A1. A sketch of the immersed boundary method depicted within the cartesian grid of the LES.

A signed-distance function $\varphi(\boldsymbol{x})$ is used to denote the solid-fluid interface ($\varphi = 0$), separating grid points within the solid ($\varphi < 0$) from those within the fluid ($\varphi > 0$). Because this implementation of the LES is not wall-resolving, the stress must be specified by a wall model at grid points adjacent to the solid-fluid interface (wall surface). The adjacent grid points in current IBM formulation are defined as all the points within the thin band $|\varphi| < \delta$, where $\delta = 1.1\Delta z$ and Δz is the vertical grid spacing (see Figure A1). For each grid point within this band, the wall stress based on a local coordinate system is calculated by the following steps:

1. The normal vector $\boldsymbol{n}^* = \boldsymbol{e}_3^*$ to the topography surface is calculate from the signed-distance function φ via

$$\boldsymbol{e}_3^* = \frac{\nabla\varphi}{|\nabla\varphi|} \,. \tag{1}$$

The velocity vector $\boldsymbol{u}$ at the point which is $h_u = 1.5\Delta z$ along the normal direction $\boldsymbol{e_3^*}$ away from the wall is calculated using trilinear interpolation.

2. This velocity $\boldsymbol{u}$ is decomposed into $\boldsymbol{u} = u_3^*\boldsymbol{e_3^*} + u_1^*\boldsymbol{e_1^*}$, where u_3^* is the component normal to surface and $u_1^* > 0$ is a residual tangential component. A local coordinate system can be defined as $(\boldsymbol{e_1^*}, \boldsymbol{e_2^*}, \boldsymbol{e_3^*})$, where $\boldsymbol{e_2^*} = \boldsymbol{e_3^*} \times \boldsymbol{e_1^*}$.

3. The wall model is used to calculate the corresponding SGS shear stress τ_{13}^* in the local coordinate system following

$$\tau_{13}^* = -\rho \left[\frac{\kappa u_1^*}{\ln(h_u/z_0)} \right]^2 , \tag{2}$$

where z_0 is the roughness length of the solid-fluid interface, and $\kappa = 0.4$ is the von Kàrmàn constant. Due to the symmetry of the stress tensor we have $\tau_{31}^* = \tau_{13}^*$.

4. The wall stress is transformed back into the original Cartesian coordinate system of the simulation via

$$\tau_{ij} = a_{in} a_{mj} \tau_{nm}^* , \tag{3}$$

where a_{ij} is the direction cosine between the original x_i-axis and the rotated x_i^*-axis.

In addition to using the wall model described above to determine the stresses within the thin band, the velocity field within the solid portion of the domain is set to zero. This in turn creates strong discontinuities in the velocity field, which are problematic for the determination of the horizontal derivatives within the pseudo-spectral approach. To reduce the Gibbs oscillations, cubic interpolations are performed within the solid region to smooth the sharp gradients prior to the transformation into Fourier space (Li et al. 2016).

We have performed one detailed validation of this IBM implementation by comparing results from our LES code to a high-resolution, wall-resolving LES using curvilinear coordinates performed by Gloerfelt and Cinnella (2019). This comparison is reported in the appendix of Heisel et al. (2021). The simulation features a periodic repetition of a single hill with a non-trivial shape (i.e., not a simple cosine) that has been extensively used as a test case in the literature because it is a challenging case with steep slopes and flow separation that has extensive documentation from DNS (Krank et al. 2018) and water flume experiments (Rapp and Manhart 2011). While this is only one case, it helps build trust in our implementation. In addition, many studies using the same implementation of the IBM in slightly different pseudo-spectral codes have performed validation in different geometries including urban buildings (e.g., Tseng et al. 2006; Giometto et al. 2016; Lin et al. 2020) and topography (e.g., Diebold et al. 2013). In general, the IBM method can accurately reproduce the effects of topography if the grid is fine enough.

APPENDIX B

Domain size and grid resolution for LES

The selection of domain and grid size in LES always requires careful considerations in order to produce accurate simulation results at affordable computational cost. Here we first justify our choice of domain size and then grid resolution, even though these decisions are obviously coupled by the constraint of computational cost.

The domain height L_z used in our simulations varies from 515 to 540 m, which is similar to typical values of ABL height observed over the Amazon forest in the morning and early afternoon, but significantly less than the mid-afternoon peak around 1200 m (Fisch et al. 2004; Dias-Júnior et al. 2019). In addition, our focus is on the flow in the roughness sublayer, roughly defined as $Z/h_c \leq 2$, and the question is whether the flow in this region is impacted by the limited domain height. For the flat case, a vertical domain size $L_z/h_c \geq 10$ is sufficient to guarantee that the roughness sublayer is not impacted by the top boundary condition (Pan and Chamecki 2016) and doubling the domain size from $10h_c$ to $20h_c$ produces negligible differences in the results (Bailey and Stoll 2016), suggesting that our choice of $L_z/h_c \approx 13.2$ is adequate. For the ideal topography, we estimate the middle layer height (Hunt et al. 1988; Finnigan and Belcher 2004) to be $h_m \approx 108$ m, and set $L_z = 5h_m$ to guarantee that the upper half of the domain is in the outer layer and the vertical velocity perturbation induced by the topography is close to zero in this region. Note that in our setup this criterion results in a larger vertical domain size than the $L_z = \lambda/3$ (where $\lambda = 1000$ m is the topography wavelength) recommended by Wood (2000) for flow over sinusoidal hills. For the horizontal domain size, the critical issue is to ensure that the domain is large enough to represent the largest eddies, which is done by assessing the two-point autocorrelations for each velocity component (Moin and Kim 1982). Our choice of $L_x \approx 3.7L_z$ and $L_y \approx 1.9L_z$ is enough to guarantee that, and it is more conservative than the recommendation of Mason and Thomson (1987) for neutral ABLs and endorsed by Wood (2000) for flow over topography. We also note that our domain is comparable to or larger than most simulations of flow over idealized forested ridges (Ross 2008; Patton and Katul 2009). For the real simulation, our horizontal domain is extended to $L_x = L_z = 3000\,\mathrm{m} \approx 5.6L_z$. This choice is mostly based on the topography characteristics, and it was selected to encompass the largest features observed at this location (i.e., without artificially reducing the size of hills, ridges, or valleys). Because of periodic boundary conditions implied by the pseudo-spectral discretization, our simulation is representative of a large area in which the topography has very similar characteristics to those present within our domain (as opposed to a region in which our real topography sits in the middle of a flat area).

Our selection of grid resolution and grid aspect ratio are also based on assumption that the critical component is the representation of the canopy shear layer eddies, which are responsible for most of the transport of gases and momentum across the canopy top (Raupach et al. 1996; Finnigan 2000). These eddies have a length scale approximately equal to the shear length scale $L_s = \overline{u}(h_c)/(\partial\overline{u}/\partial z)_{h_c}$, and are spaced in the horizontal direction by a distance of roughly $8L_s$ (Raupach et al. 1996). From our canopy simulation over flat topography we obtain $L_s \approx 30\,\mathrm{m}$, so that our grid size is $\Delta x \approx 0.21L_s$ and $\Delta z \approx 0.07L_s$ (shear layer eddies are resolved by roughly 5 points in the horizontal direction and 15 points in the vertical; note that the finite-difference discretization in the vertical requires more points to resolve flow structures than the spectral discretization in the horizontal directions). To accommodate the larger horizontal domain in the simulation with real topography, we use a slightly large horizontal grid spacing so that $\Delta x \approx 0.27L_s$ and eddies are resolved by roughly 4 grid points (the vertical resolution is not altered). Our resolution is slightly better than that used by Ross (2008). While most papers reporting flow within canopies over topography do not report the ratio of grid size to L_s, our resolution normalized by the canopy height ($\Delta x \approx 0.16h_c$ to $\Delta x \approx 0.21h_c$ and $\Delta z \approx 0.05h_c$) is comparable or higher than most studies (as examples, Dupont et al. (2008) uses $\Delta x = 0.6h_c$ and $\Delta z = 0.2h_c$, Patton and Katul (2009) uses $\Delta x \approx 0.15h_c$ and $\Delta z = 0.05h_c$, Ross (2011) uses $\Delta x = \Delta z \approx 0.14h_c$, and Ma et al. (2020) uses $\Delta x = 0.3h_c$ and $\Delta z = 0.1h_c$). Note that Ouwersloot et al. (2017) performed tests of model resolution for flow within canopies over flat terrain using a finite-difference code and found small differences between their reference simulation following Finnigan et al. (2009) with $\Delta x = \Delta z = 0.1h_c$ and a test simulation with $\Delta x = 0.2h_c$ (keeping Δz the same), concluding that the latter is not sufficient. However, our spectral code should be able to represent smaller scales in comparison to a finite-difference code at the same grid resolution, and we conclude that our choice is reasonable. For our setup, this requirement of resolving eddies of size L_s will automatically ensure that the idealized ridge is well resolved, and that the larger features in the real topography are well resolved. The smaller bumps and dips in the real topography are likely under-resolved, even though our simulation can capture the recirculation in the wake of most small bumps (e.g., see Figure 2a in Chen et al. (2020)).

APPENDIX C

TKE budget over crests and troughs

For clarity, we include here the definition used to separate the TKE budget into vertical and horizontal components when analyzing results over flat terrain, crests and troughs. In practice, Equation (2) of the main text can be written as

$$\frac{\partial \overline{e}}{\partial t} = A_e^h + A_e^v + P^h + P^v + \Pi_e^h + \Pi_e^v + T_e^h + T_e^v - \epsilon_c - \epsilon, \tag{C1}$$

and each term on the right-hand side is defined below:

$$A_e^h = -\frac{\partial \overline{\widetilde{u}}\,\overline{e}}{\partial x} - \frac{\partial \overline{\widetilde{v}}\,\overline{e}}{\partial y} \tag{C2}$$

$$A_e^v = -\frac{\partial \overline{\widetilde{w}}\,\overline{e}}{\partial z} \tag{C3}$$

$$\begin{aligned} P^h = &-\overline{\widetilde{u}'\widetilde{u}'}\frac{\partial \overline{\widetilde{u}}}{\partial x} - \overline{\widetilde{u}'\widetilde{v}'}\frac{\partial \overline{\widetilde{u}}}{\partial y} - \overline{\widetilde{u}'\widetilde{v}'}\frac{\partial \overline{\widetilde{v}}}{\partial x} \\ &- \overline{\widetilde{v}'\widetilde{v}'}\frac{\partial \overline{\widetilde{v}}}{\partial y} - \overline{\widetilde{u}'\widetilde{w}'}\frac{\partial \overline{\widetilde{w}}}{\partial x} - \overline{\widetilde{v}'\widetilde{w}'}\frac{\partial \overline{\widetilde{w}}}{\partial y} \end{aligned} \tag{C4}$$

$$P^v = -\overline{\widetilde{u}'\widetilde{w}'}\frac{\partial \overline{\widetilde{u}}}{\partial z} - \overline{\widetilde{v}'\widetilde{w}'}\frac{\partial \overline{\widetilde{v}}}{\partial z} \tag{C5}$$

$$\Pi_e^h = -\frac{\partial \overline{\widetilde{p}^{*\prime}\widetilde{u}'}}{\partial x} - \frac{\partial \overline{\widetilde{p}^{*\prime}\widetilde{v}'}}{\partial y} \tag{C6}$$

$$\Pi_e^v = -\frac{\partial \overline{\widetilde{p}^{*\prime}\widetilde{w}'}}{\partial z} \tag{C7}$$

$$\begin{aligned} T_e^h = &-\frac{\partial \overline{\widetilde{u}'e}}{\partial x} - \frac{\partial \overline{\widetilde{u}'(\tau'_{xx}+\tau'_{xy}+\tau'_{xz})}}{\partial x} \\ &- \frac{\partial \overline{\widetilde{v}'e}}{\partial y} - \frac{\partial \overline{\widetilde{v}'(\tau'_{xy}+\tau'_{yy}+\tau'_{yz})}}{\partial y} \end{aligned} \tag{C8}$$

$$T_e^v = -\frac{\partial \overline{\widetilde{w}'e}}{\partial z} - \frac{\partial \overline{\widetilde{w}'(\tau'_{xz}+\tau'_{yz}+\tau'_{zz})}}{\partial z} \tag{C9}$$

References

Albertson, J. D., and M. B. Parlange, 1999: Surface length scales and shear stress: Implications for land-atmosphere interaction over complex terrain. *Water Resources Research*, **35 (7)**, 2121–2132.

Aubinet, M., B. Heinesch, and M. Yernaux, 2003: Horizontal and vertical CO2 advection in a sloping forest. *Boundary-Layer Meteorology*, **108 (3)**, 397–417.

Bailey, B. N., and R. Stoll, 2016: The creation and evolution of coherent structures in plant canopy flows and their role in turbulent transport. *Journal of Fluid Mechanics*, **789**, 425–460.

Belcher, S. E., T. Newley, and J. Hunt, 1993: The drag on an undulating surface induced by the flow of a turbulent boundary layer. *Journal of Fluid Mechanics*, **249**, 557–596.

Bou-Zeid, E., C. Meneveau, and M. Parlange, 2005: A scale-dependent Lagrangian dynamic model for large eddy simulation of complex turbulent flows. *Physics of Fluids*, **17 (2)**, 025 105.

Brown, A. R., J. Hobson, and N. Wood, 2001: Large-eddy simulation of neutral turbulent flow over rough sinusoidal ridges. *Boundary-Layer Meteorology*, **98 (3)**, 411–441.

Brunet, Y., J. Finnigan, and M. Raupach, 1994: A wind tunnel study of air flow in waving wheat: single-point velocity statistics. *Boundary-Layer Meteorology*, **70 (1)**, 95–132.

Chamecki, M., N. L. Dias, and L. S. Freire, 2018: A TKE-based framework for studying disturbed atmospheric surface layer flows and application to vertical velocity variance over canopies. *Geophysical Research Letters*, **45 (13)**, 6734–6740.

Chamecki, M., and Coauthors, 2020: Effects of vegetation and topography on the boundary layer structure above the amazon forest. *Journal of the Atmospheric Sciences*, **77 (8)**, 2941–2957.

Chen, B., M. Chamecki, and G. G. Katul, 2019: Effects of topography on in-canopy transport of gases emitted within dense forests. *Quarterly Journal of the Royal Meteorological Society*, **145 (722)**, 2101–2114.

Chen, B., M. Chamecki, and G. G. Katul, 2020: Effects of gentle topography on forest-atmosphere gas exchanges and implications for eddy-covariance measurements. *Journal of Geophysical Research: Atmospheres*, **125 (11)**, e2020JD032 581.

Chester, S., C. Meneveau, and M. B. Parlange, 2007: Modeling turbulent flow over fractal trees with renormalized numerical simulation. *Journal of Computational Physics*, **225 (1)**, 427–448.

Dias-Júnior, C. Q., and Coauthors, 2019: Is there a classical inertial sublayer over the amazon forest? *Geophysical Research Letters*, **46 (10)**, 5614–5622.

Diebold, M., C. Higgins, J. Fang, A. Bechmann, and M. B. Parlange, 2013: Flow over hills: a large-eddy simulation of the bolund case. *Boundary-layer meteorology*, **148 (1)**, 177–194.

Dupont, S., Y. Brunet, and J. Finnigan, 2008: Large-eddy simulation of turbulent flow over a forested hill: Validation and coherent structure identification. *Quarterly Journal of the Royal Meteorological Society*, **134 (636)**, 1911–1929.

Dwyer, M. J., E. G. Patton, and R. H. Shaw, 1997: Turbulent kinetic energy budgets from a large-eddy simulation of airflow above and within a forest canopy. *Boundary-Layer Meteorology*, **84 (1)**, 23–43.

Finnigan, J., 2000: Turbulence in plant canopies. *Annual review of fluid mechanics*, **32 (1)**, 519–571.

Finnigan, J. J., and S. E. Belcher, 2004: Flow over a hill covered with a plant canopy. *Quarterly Journal of the Royal Meteorological Society*, **130 (596)**, 1–29, https://doi.org/10.1256/qj.02.177.

Finnigan, J. J., R. H. Shaw, and E. G. Patton, 2009: Turbulence structure above a vegetation canopy. *Journal of Fluid Mechanics*, **637**, 387–424.

Fisch, G., J. Tota, L. Machado, M. Silva Dias, R. da F Lyra, C. Nobre, A. Dolman, and J. Gash, 2004: The convective boundary layer over pasture and forest in amazonia. *Theoretical and Applied Climatology*, **78 (1)**, 47–59.

Fuentes, J. D., and Coauthors, 2016: Linking meteorology, turbulence, and air chemistry in the amazon rain forest. *Bulletin of the American Meteorological Society*, **97 (12)**, 2329–2342.

Gerken, T., M. Chamecki, and J. D. Fuentes, 2017: Air-parcel residence times within forest canopies. *Boundary-Layer Meteorology*, **165 (1)**, 29–54.

Giometto, M., A. Christen, C. Meneveau, J. Fang, M. Krafczyk, and M. Parlange, 2016: Spatial characteristics of roughness sublayer mean flow and turbulence over a realistic urban surface. *Boundary-Layer Meteorology*, **160 (3)**, 425–452.

Gloerfelt, X., and P. Cinnella, 2019: Large eddy simulation requirements for the flow over periodic hills. *Flow, Turbulence and Combustion*, **103 (1)**, 55–91.

Heisel, M., B. Chen, J. F. Kok, and M. Chamecki, 2021: Gentle topography increases vertical transport of coarse dust by orders of magnitude. *Journal of Geophysical Research: Atmospheres*, **126 (14)**, e2021JD034 564.

Hunt, J., S. Leibovich, and K. Richards, 1988: Turbulent shear flows over low hills. *Quarterly Journal of the Royal Meteorological Society*, **114 (484)**, 1435–1470.

Jackson, P., 1981: On the displacement height in the logarithmic velocity profile. *Journal of fluid mechanics*, **111**, 15–25.

Kaimal, J. C., and J. J. Finnigan, 1994: *Atmospheric boundary layer flows: their structure and measurement*. Oxford university press.

Katul, G., J. Finnigan, D. Poggi, R. Leuning, and S. Belcher, 2006: The influence of hilly terrain on canopy-atmosphere carbon dioxide exchange. *Boundary-Layer Meteorology*, **118 (1)**, 189–216.

Krank, B., M. Kronbichler, and W. A. Wall, 2018: Direct numerical simulation of flow over periodic hills up to $re_h = 10,595$. *Flow, turbulence and combustion*, **101 (2)**, 521–551.

Kruijt, B., Y. Malhi, J. Lloyd, A. Norbre, A. Miranda, M. G. Pereira, A. Culf, and J. Grace, 2000: Turbulence statistics above and within two amazon rain forest canopies. *Boundary-Layer Meteorology*, **94 (2)**, 297–331.

Lenschow, D., J. C. Wyngaard, and W. T. Pennell, 1980: Mean-field and second-moment budgets in a baroclinic, convective boundary layer. *Journal of the Atmospheric Sciences*, **37 (6)**, 1313–1326.

Li, Q., E. Bou-Zeid, and W. Anderson, 2016: The impact and treatment of the gibbs phenomenon in immersed boundary method simulations of momentum and scalar transport. *Journal of Computational Physics*, **310**, 237–251.

Lilly, D. K., 1967: The representation of small scale turbulence in numerical simulation experiments. *IBM Scientific Computing Symposium on environmental sciences*, Yorktown heights, 195–210.

Lin, X., M. Chamecki, G. Katul, and X. Yu, 2018: Effects of leaf area index and density on ultrafine particle deposition onto forest canopies: A LES study. *Atmospheric Environment*, **189**, 153–163.

Lin, X., M. Chamecki, and X. Yu, 2020: Aerodynamic and deposition effects of street trees on pm2. 5 concentration: From street to neighborhood scale. *Building and Environment*, **185**, 107 291.

Ma, Y., H. Liu, T. Banerjee, G. G. Katul, C. Yi, and E. R. Pardyjak, 2020: The effects of canopy morphology on flow over a two-dimensional isolated ridge. *Journal of Geophysical Research: Atmospheres*, **125 (19)**, e2020JD033 027.

Mason, P. J., and D. Thomson, 1987: Large-eddy simulations of the neutral-static-stability planetary boundary layer. *Quarterly Journal of the Royal Meteorological Society*, **113 (476)**, 413–443.

Mittal, R., and G. Iaccarino, 2005: Immerse boundary methods. *Annual Review of Fluid Mechanics*, **37 (1)**, 239–261.

Moin, P., and J. Kim, 1982: Numerical investigation of turbulent channel flow. *Journal of fluid mechanics*, **118**, 341–377.

Ouwersloot, H., A. Moene, J. Attema, and J. de Arellano, 2017: Large-eddy simulation comparison of neutral flow over a canopy: Sensitivities to physical and numerical conditions, and similarity to other representations. *Boundary-Layer Meteorology*, **162 (1)**, 71–89.

Pan, Y., and M. Chamecki, 2016: A scaling law for the shear-production range of second-order structure functions. *Journal of Fluid Mechanics*, **801**, 459–474.

Pan, Y., M. Chamecki, and S. A. Isard, 2014: Large-eddy simulation of turbulence and particle dispersion inside the canopy roughness sublayer. *Journal of Fluid Mechanics*, **753**, 499–534.

Patton, E. G., and G. G. Katul, 2009: Turbulent pressure and velocity perturbations induced by gentle hills covered with sparse and dense canopies. *Boundary-layer meteorology*, **133 (2)**, 189–217.

Peskin, C. S., 1972: Flow patterns around heart valves: A numerical method. *Journal of Computational Physics*, **10 (2)**, 252–271.

Poggi, D., and G. G. Katul, 2007: Turbulent flows on forested hilly terrain: the recirculation region. *Quarterly Journal of the Royal Meteorological Society*, **133 (625)**, 1027–1039.

Poggi, D., G. G. Katul, J. J. Finnigan, and S. E. Belcher, 2008: Analytical models for the mean flow inside dense canopies on gentle hilly terrain. *Quarterly Journal of the Royal Meteorological Society*, **134 (634)**, 1095–1112.

Rapp, C., and M. Manhart, 2011: Flow over periodic hills: an experimental study. *Experiments in fluids*, **51 (1)**, 247–269.

Raupach, M., and A. S. Thom, 1981: Turbulence in and above plant canopies. *Annual Review of Fluid Mechanics*, **13 (1)**, 97–129.

Raupach, M. R., J. J. Finnigan, and Y. Brunet, 1996: Coherent eddies and turbulence in vegetation canopies: the mixing-layer analogy. *Boundary-layer meteorology 25th anniversary volume, 1970–1995*, Springer, 351–382.

Ross, A. N., 2008: Large-eddy simulations of flow over forested ridges. *Boundary-layer meteorology*, **128 (1)**, 59–76.

Ross, A. N., 2011: Scalar transport over forested hills. *Boundary-Layer Meteorology*, **141 (2)**, 179–199.

Ross, A. N., and I. N. Harman, 2015: The impact of source distribution on scalar transport over forested hills. *Boundary-Layer Meteorology*, **156 (2)**, 211–230, https://doi.org/10.1007/s10546-015-0029-5.

Ross, A. N., and S. B. Vosper, 2005: Neutral turbulent flow over forested hills. *Quarterly Journal of the Royal Meteorological Society*, **131 (609)**, 1841–1862, https://doi.org/10.1256/qj.04.129.

Ruck, B., and E. Adams, 1991: Fluid mechanical aspects of the pollutant transport to coniferous trees. *Boundary-Layer Meteorology*, **56 (1-2)**, 163–195.

Santana, R. A., C. Q. Dias-Júnior, J. T. da Silva, J. D. Fuentes, R. S. do Vale, E. G. Alves, R. M. N. dos Santos, and A. O. Manzi, 2018: Air turbulence characteristics at multiple sites in and above the amazon rainforest canopy. *Agricultural and Forest Meteorology*, **260**, 41–54.

Shaw, R. H., and U. Schumann, 1992: Large-eddy simulation of turbulent flow above and within a forest. *Boundary-Layer Meteorology*, **61 (1-2)**, 47–64.

Smagorinsky, J., 1963: General circulation experiments with the primitive equations: I. the basic experiment*. *Monthly weather review*, **91 (3)**, 99–164.

Tamura, T., A. Okuno, and Y. Sugio, 2007: Les analysis of turbulent boundary layer over 3d steep hill covered with vegetation. *Journal of Wind Engineering and Industrial Aerodynamics*, **95 (9-11)**, 1463–1475.

Tóta, J., D. R. Fitzjarrald, and M. A. F. da Silva Dias, 2012: Amazon rainforest exchange of carbon and subcanopy air flow: Manaus LBA site—a complex terrain condition. *The Scientific World Journal*, **2012**, 1–19.

Tseng, Y.-H., C. Meneveau, and M. B. Parlange, 2006: Modeling flow around bluff bodies and predicting urban dispersion using large eddy simulation. *Environmental science & technology*, **40 (8)**, 2653–2662.

Wood, N., 2000: Wind flow over complex terrain: a historical perspective and the prospect for large-eddy modelling. *Boundary-Layer Meteorology*, **96 (1)**, 11–32.

Wood, N., and P. Mason, 1993: The pressure force induced by neutral, turbulent flow over hills. *Quarterly Journal of the Royal Meteorological Society*, **119 (514)**, 1233–1267.

Yue, W., C. Meneveau, M. B. Parlange, W. Zhu, H. S. Kang, and J. Katz, 2008: Turbulent kinetic energy budgets in a model canopy: comparisons between les and wind-tunnel experiments. *Environmental Fluid Mechanics*, **8 (1)**, 73–95.